CrossMark

Numerical Modeling of Flow Over Two Side Weirs

Mohammad Reza Namaee[1] · Reyhane Shadpoorian[2]

Abstract Nowadays, due to the significant development of hydraulic models, it is possible to investigate miscellaneous hydraulic phenomena and reveal the extent to which their changes in a particular parameter will affect the flow condition without the need of extra experiments. In the present study, flow patterns over a side weir were studied both experimentally and numerically. The experiments were done for a side weir with the length of 4 m. However, in the numerical model, the 4 m weir was replaced with two side weirs with the length of 2 m which were placed within two meters distance from each other. The primary contributions of the paper are to show that a numerical model can be used to simulate the flow over both single and double side weirs, and to quantify the increased discharge from two side weirs relative to discharge from a single side weir having the same crest length as the two side weirs.

List of symbols

B Main width of the channel
L Side weir length
E Specific energy

✉ Mohammad Reza Namaee
  mnamaee@unbc.ca

  Reyhane Shadpoorian
  rshadpoorian@yahoo.com

1   Natural Resources and Environmental Studies, University of Northern British Columbia, Prince George, Canada

2   Department of Civil Engineering, Khaje Nasir Toosi University of Technology, Tehran, Iran

Q_1 Inlet discharge
Q_2 Downstream discharge
Q_{31} First weir outflow discharge
Q_{32} Second weir outflow discharge
Q_3 Total weir outflow discharge
Fr   Froude number
P Side weir height
y_1 Upstream water depth in main channel
y_C Critical water depth in main channel

1 Introduction

Side weirs have been used widely in irrigation, land drainage and urban sewage systems as a diversion system and are most normally aligned parallel to the channel or river wall. Side weirs are one of the major parts of floodwater spreading systems. Their crucial task is to broaden floodwater and to amplify its penetration into the ground. Figure 1 shows a satellite photo of the Garabaygan Plain. Garabaygan Plain (28°30′ to 28°45′N and 53°45′ to 54°01′E) is located in the south part of Fars province of Iran

The mean elevation of the area is 1476 m above mean sea level. According to the De Martonne [1] aridity index, the area represents a dry climate type with the average annual rainfall of 259 mm, the average annual potential evaporation rate of 2934 mm, and the average annual temperature of 20.6 °C. In Garabaygan Plain, floodwater spreading systems are used to reduce the destructive effects of floods and also provide new water resources for various uses. Figure 2 shows a detailed satellite photo of the floodwater spreading systems used in Garabaygan Plain.

The passage of flow through channels is shown with blue arrows, and the passage of flow from upstream of the floodwater system toward the downstream of the floodwater

🍂 Springer

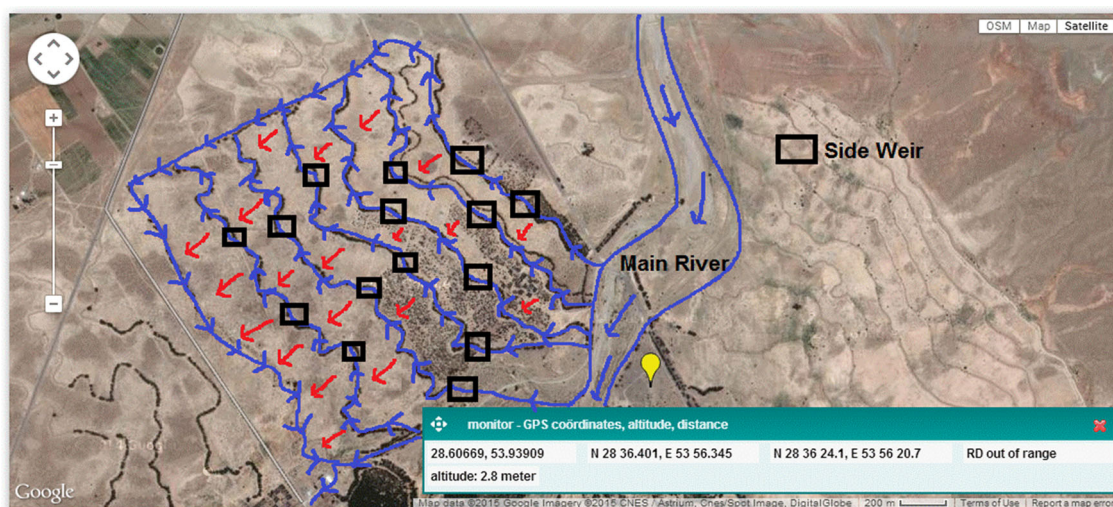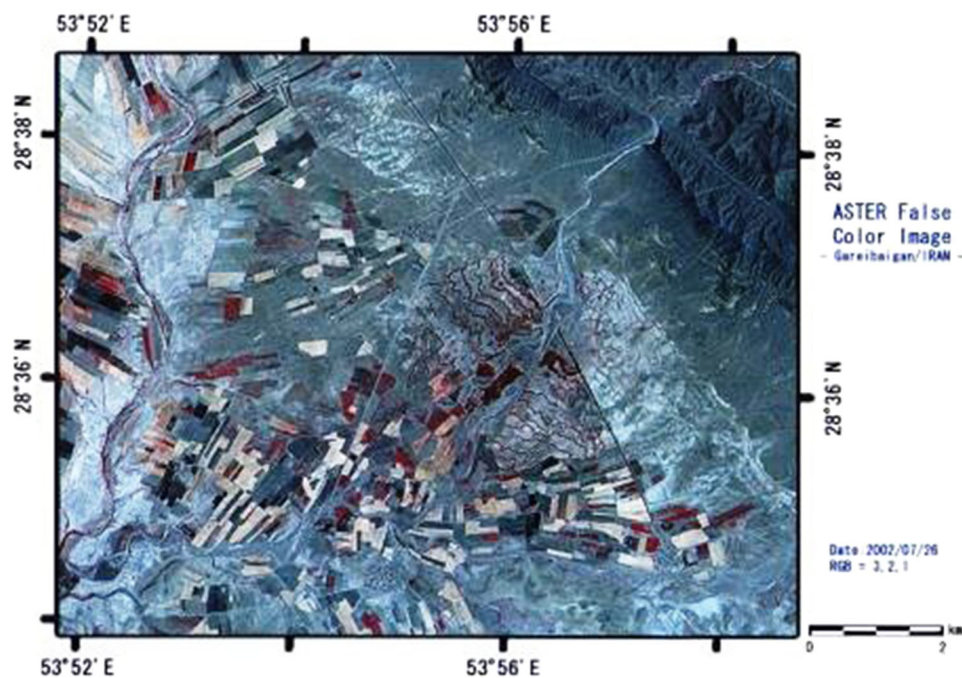**Fig. 1** A satellite photo of the Garabaygan Plain

Fig. 2 A detailed satellite photo of the floodwater spreading systems used in Garabaygan Plain

spreading system is shown with red arrows. The locations of the side weirs through which the flow passes toward the downstream of the system are shown with black rectangular. Flood water spreading system is an effective and appropriate method for optimization of runoff utilization, particularly in arid and semiarid regions. They are designed for artificial recharge of groundwater and for improving groundwater quality in the region. In this case, when the runoff in the river overflows, it will be diverted into the watershed system through regulation facilitates. Afterward, if approaching flow in the channel is potential to overflow, a portion of the flow will be diverted to the next downstream channel by means of side weirs. In other words, a side weir can be used as the structure that diverts surplus discharges from the main channel into the next channel. During this process, the destructive power of the flood will decrease considerably. Beside the reduction in flood damage, this technique is also useful for artificial recharge, rangeland rehabilitation and desertification control.

Therefore, the application and characteristics of flow over the side weirs should be thoroughly understood. Side weirs have attracted considerable interest among significant researchers due to various applications and also different types of possible flow conditions. The most important issue associated with the side weirs is the amount of discharge that can be overflowed to the side channel. Estimation of dis-

charge over the side weirs is a main issue and a continuing problem in the area of water measurement yet.

Most of the studies on side weirs were focused on the empirical derivation of discharge formulas before 1978. Perhaps, the first rational approach to study side weir discharge was proposed by De Marchi [2], who developed an equation for the water profile across a side weir on the assumption that total energy along the side weir is constant. A review of previous studies indicated that rectangular sharp-crested side weirs have been investigated extensively, including work by Ackers [3], Collings [4], Frazer [5], Subramanya and Awasthy [6], Nandesamoorthy and Thomson [7], Singh et al. [8], Yu-Tech [9], Cheong [10]. El-Khashab and Smith [11], Uyumaz and Muslu [12], Hager [13,14], Helweg [15], Agaccioglu and Yüksel [16], Venutelli [17] and Durga Rao and Pillai [18]. Ranga Raju et al. [19] investigated the discharge coefficient of a broad-crested rectangular side weir, based on the width of the main channel and Froude number. They reported for their experiments that the specific energy remained nearly constant with the maximum difference being $<2\%$. Kumar and Pathak [20] investigated the discharge coefficient of sharp and broad-crested triangular side weirs. Hager [13] discussed the fact that, when one-dimensional analysis is used, the hydraulic characteristics of side weir flow cause an additional head change that may be either positive or negative, depending on the flow conditions. Borghei et al. [21] studied the discharge coefficient for sharp-crested side weirs in subcritical flow and developed an equation for the discharge coefficient of sharp-crested rectangular side weirs. Kaya et al. [22] investigated the hydraulic effects of semi-elliptical side weirs in order to increase their discharge capacity. They conducted a comprehensive study, including 677 tests to determine the discharge coefficient of the semi-elliptical side weir. They found that the discharge coefficient of semi-elliptical side weirs was higher than that of classical side weirs. It was perceived that in most of the fundamental research about side weir coefficient in subcritical condition, upstream Froude number is introduced as the main dimensionless parameter and the proposed equations are based on the variation of the upstream Froude number. However, Singh et al. [8] has introduced (P/y_1) as another effective parameter on side weir coefficient. It should be mentioned that P represents side weir height and y_1 represents the upstream flow depth. Borghei et al. [21] have concluded that for a more accurate equation to predict discharge coefficient of side weir, the effects of the upstream Froude number (P/y_1) and (L/B) should be considered all together. It should be mentioned that L represents side weir length and B represents main channel width. Namaee et al. [23] investigated a long broad-crested side weir in a trapezoidal channel with significant rough bed under subcritical condition. They proposed an equation for discharge coefficient of side weirs based on their experiments and they compared it to other

significant empirical equations. They concluded that due to many special factors affecting the discharge coefficient, the experimental discharge coefficient was much less than the predicted ones purposed by other empirical equations.

Today, with the availability of powerful numerical models, we can study flow over the side weirs and consequently estimate the outflow discharge. Isel et al. [24] developed a CFD-based methodology to assess the overflow discharge and the related uncertainties using measurements of the water depth in sewage networks and especially in nonstandard combined sewer overflows (CSOs) with the finite volume code ANSYS-FLUENT. This general method to calculate the discharge using water level measurements presented several advantages. Firstly, an estimation of the related uncertainty takes into account the numerical error, the regression error and the measurement uncertainty in the determination of a suitable height–discharge relationship. Secondly, their methodology enables sewer manager to answer to the operational limitation of self-monitoring by calculating the over-flow volumes and their related uncertainties. Chen et al. [25] developed a 3D model to optimize urban sewer design and consequently minimize emissions into receiving water body. The 3D free water surface model adopted the renormalized group (RNG), k-ε turbulence model and the volume of fluid (VOF). The particle tracking approach was used in order to compare the predicted flow field data with the measurements in laboratory-scale experiments. This study indicates that the developed 3D numerical model is a useful approach to design lucrative urban sewage systems, to optimize existing urban sewage systems and also to reduce the direct discharges of suspended particles and a variety of water pollutants into the receiving water body. Isel et al. [26] developed a CFD model to assess the relationship between discharge and water depth for combined sewer overflows (CSO) chambers. Their technique is particularly appropriate for complex geometries and complex downstream hydraulic conditions. This study focuses on the assessment and integration of the uncertainties in the determination of the most suitable depth–overflow relationship. This approach was exemplified through the case of the 'Milan' CSO of Mulhouse city, France. Lipeme Kouyi et al. [27] used 3D modeling and several ultrasound sensors to determine the overflow rate of five complex CSOs of the system in Se'lestat (French). They established self-monitoring on the system in Se'lestat with the help of a new instrumentation mode involving several ultrasound sensors. In their study, it is obvious that how 3D and 1D models have made it possible to predict the shapes of the water lines and suggest a location for the ultrasound sensors. Namaee et al. [28] numerically investigated flow over a broad-crested side weir. They concluded that the numerical model was capable of simulating this phenomenon to a satisfactory extent except at the upper section of the side weir where the flow diverts into the side weir. In this loca-

tion, due to the collision between the flow and the earthen materials, a part of the lateral wall would be eroded in the experiments; however, in the numerical model, this part was assumed to be rigid. Nevertheless, their simulation results provided detailed analysis of flow pattern, pressure distributions in longitudinal and transverse sections over the side weir at the specified locations. In another study, in order to consider the effect of eroded part of the upper section of the side weir in the numerical model, Namaee [29] eliminated the certain area in the numerical model. It was concluded that after elimination of the eroded part from the numerical model, experimental and numerical data were much closer to one another.

As the numerical result of Namaee et al. [28] and Namaee [29] was in a relatively good agreement with the experimental one, the present work studies another numerical model based on free-surface computational fluid dynamics (CFD) model in which two side weirs with the lengths of 2 m have taken the place of an experimental side weir with the length of 4 m. The objective of this study is to determine whether or not installation of two side weirs with shorter lengths will be more practical to be used in hydraulic projects. The simulation results will provide detailed analysis of flow pattern, water surface pattern in longitudinal and transverse sections and also the amount of outflow discharge over the side weirs.

1.1 Different Types of Flow Conditions Over a Side Weir

The flow conditions in the main channel at upstream and downstream of a side weir can have a major influence on the behavior of the flow at the weir itself. There are three different types of the flow that happen along the weir and can best categorized in terms of the Froude number, Fr, of the flow. In type 1, the channel is on mild slope, and the flow upstream, downstream and along the length of the side weir remains subcritical at all points. The key feature to note is that the water level in the main channel increases along the weir in the downstream direction. Therefore, the head acting on the weir is greater at the downstream end than at the upstream end. As a result, the discharge intensity of the spill flow is not constant but increases in the downstream direction (Fig. 3a). On the other hand, if the flow upstream, downstream and along the length of side weir remains supercritical at all points, (Fr > 1), then a supercritical condition occurs and the flow depth decreases to the end of the weir.

Fig. 3 **a** Longitudinal flow profile at a side weir under subcritical condition, **b** longitudinal flow profile at a side weir under super-critical condition, **c** longitudinal flow profile at a side weir under mixed flow condition
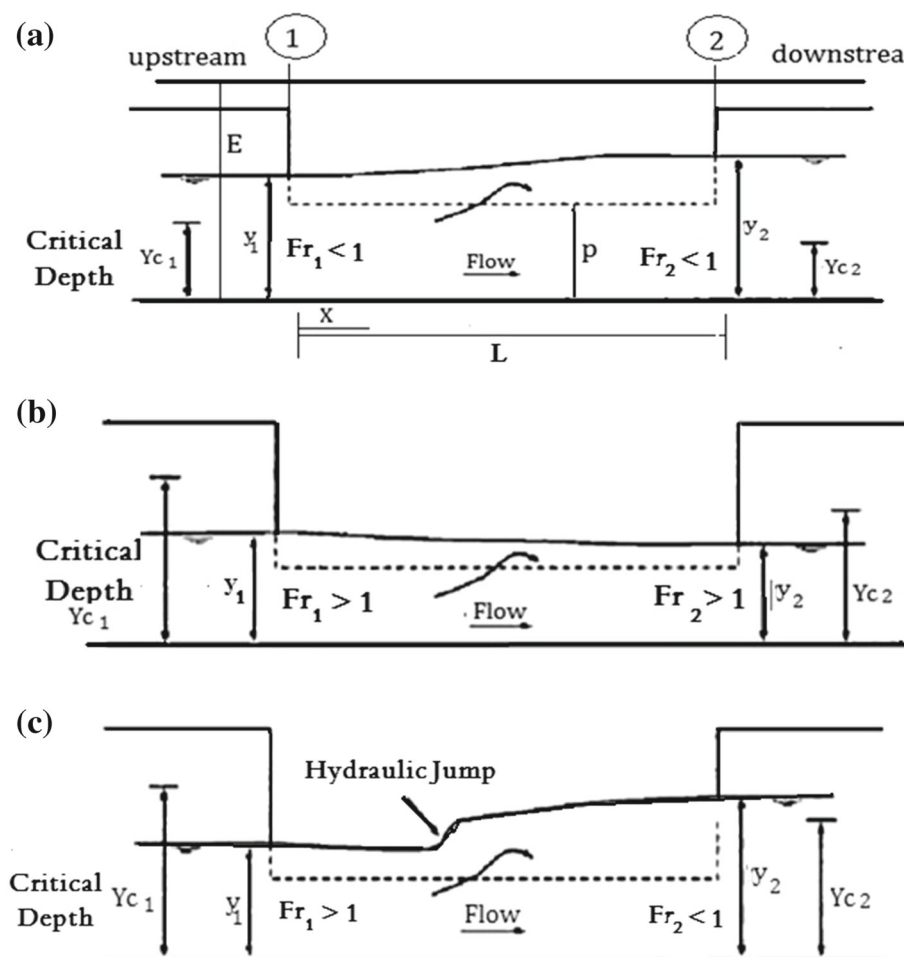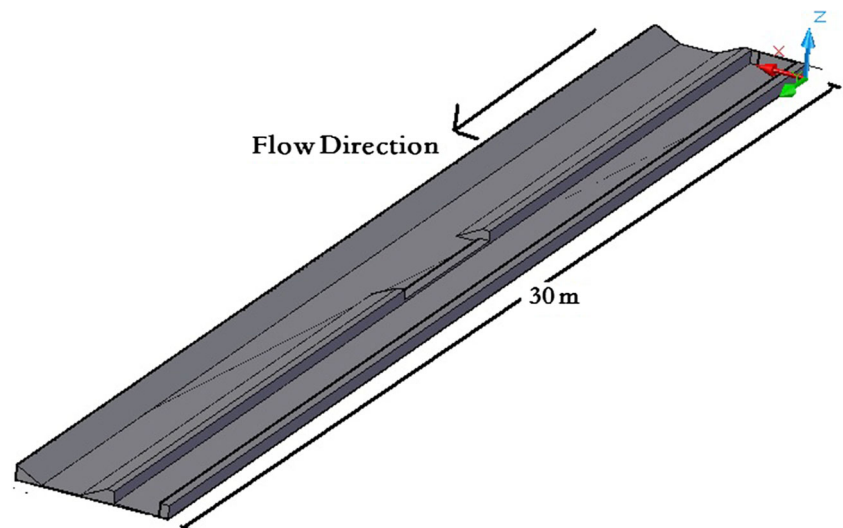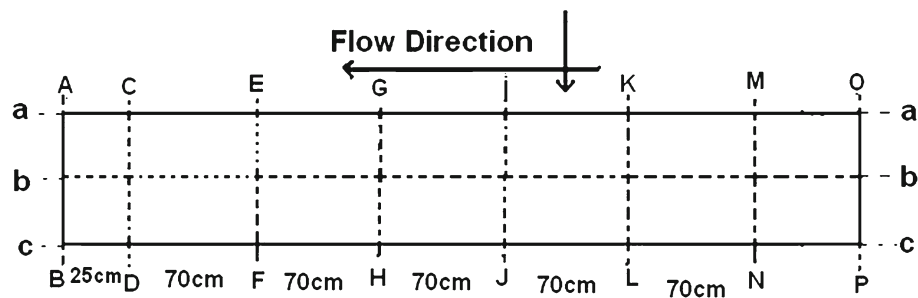
Fig. 4 Experimental setup

Fig. 5 Locations of hydrostatic pressure measurement on the weir crest

This condition can occur if the side weir is installed in a steep parent channel that is not subject to downstream regulation or control (e.g., by a gated structure or a natural constriction in the channel). As the result, the discharge intensity of the spill flow decreases toward the downstream end of the weir (Fig. 3b). Finally, if there is a discontinuity in the flow, due to the downstream depth being greater than the critical depth, a hydraulic jump is expected. This condition should be avoided because the longitudinal position of the jump can be very sensitive to changes in the flow rate or roughness of the channel. Downstream of the jump, the head over the weir and the rate of outflow are significantly greater than upstream of the jump. Therefore, if the jump is not stable, the performance of the weir will be likely to be erratic and difficult to predict or control accurately (Fig. 3c) [30]. Figure 1a is a typical design that usually happens in floodwater spreading system.

2 Experimental Setup and Measurements

The experimental setup consisted of a main channel and a lateral channel (Fig. 4). The main channel was 30 m in length, 1 m in width and 0.6 m in depth. The main channel had a trapezoidal cross section with 1H:1V side slopes. The lon-gitudinal slope of the main channel was 0.001. The lateral channel was 1.5 m wide and 0.8 m deep, and was situated parallel to the main channel. A rectangular weir was placed at the end of the lateral channel in order to measure the discharge of the side weir. A point gauge with ±0.1 mm sensitivity was placed at 0.5 m from the weir. A concrete side weir with the length of 4 m and the width of 23 cm was constructed at the distance of 12.88 m from upstream inlet. The inlet discharges were measured via a rectangular sharp-crested weir. A calibrated standard rectangular sharp-crested weir was installed at the beginning of the main channel which is used to adjust inlet flow to an accuracy of ±0.1 L/s.

Data collected include the measurements of hydrostatic pressure at different locations both in the longitudinal and in the transverse directions of flow over the crest of the side weir and in the main channel. They were measured at 25 cm from the upstream and downstream edge of the weir by means of piezometers installed at the bottom of the side weir. Figure 5 shows locations of the measured hydrostatic pressures with alphabetic letters. In order to evaluate water level, it was assumed that the pressure was hydrostatic. Figure 6 shows a photo taken from experimental hydrostatic pressure measurement over the side weir. To measure static pressure, 8 thin hoses were placed at the bottom of the side weir centerline. They were connected to eight piezometer tubes to show

Fig. 6 Experimental
hydrostatic pressure
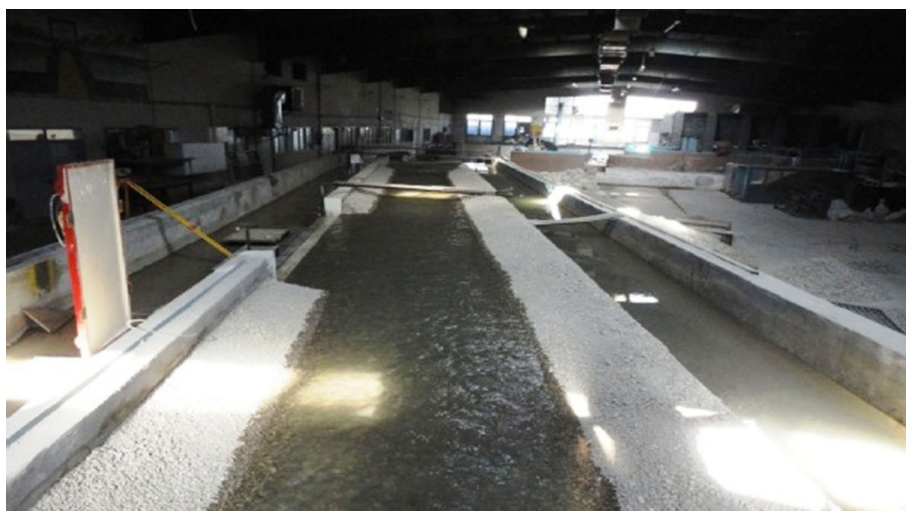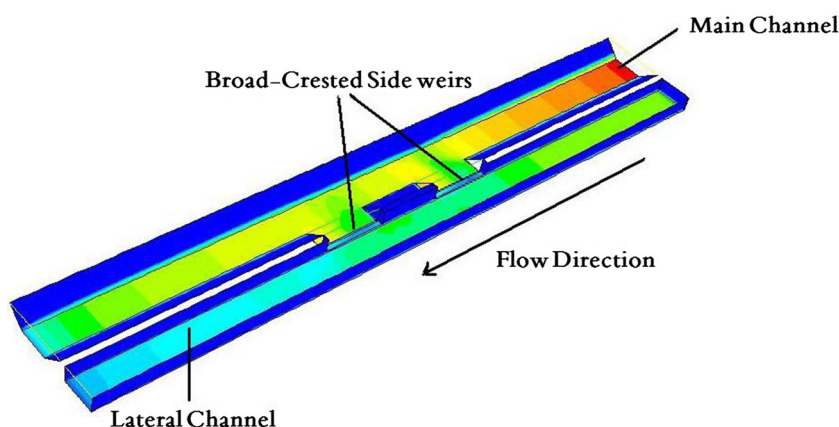measurement over the side weir

Fig. 7 A view of the simulated
side weirs

pressure head. Piezometer tubes were labeled with a ruler
with the degree of precision of 1 mm. So, the measurement
of the hydrostatic pressure was precise enough. The pressure
head can be mathematically expressed as:

$$\psi = \frac{P}{\gamma} = \frac{P}{\rho g} \tag{1}$$

where ψ is pressure head (length, typically in units of m), P is
fluid pressure (force per unit area, often as Pa units), γ is the
specific weight (force per unit volume, typically N/m^3 units),
ρ is the density of the fluid (mass per unit volume, typically
kg/m^3), g is acceleration due to gravity (rate of change of
velocity, given in m/s^2)

3 Numerical Modeling

In this study, numerical analyses are carried out by means of
FLUENT 6.3.26. FLUENT is a computational fluid dynam-
ics commercial software to simulate fluid flow problems.
The governing equations for computational fluid dynamics
(CFD) are based on conservation of mass, momentum and

energy. FLUENT uses a finite volume method (FVM) to solve
the governing equations. The FVM involves descretization
and integration of the governing equation over the control
volume. The following is a summary of applied turbulence
model as well as free surface tracking method involved
in this simulation and is based on the FLUENT User's
Manual.

3.1 *K*-epsilon (*k*-ε) Turbulence Model

K-epsilon (k-ε) turbulence model is the most common model
used in computational fluid dynamics (CFD) to simulate
mean flow characteristics for turbulent flow conditions. It
is a two-equation model which gives a general description
of turbulence by means of two transport equations (PDEs).
There are three types of k-ε turbulence model which are the
standard k-ε model, renormalization group (RNG) model and
realizable k-ε model. Since the standard k-ε is used for tur-
bulence modeling, it is introduced here for the other types
of k-ε turbulence models, please refer to FLUENT User's
Manual.

Fig. 8 Longitudinal pressure distribution profile over the side weir at axes. **a** *a–a*, **b** *b–b*, and **c** *c–c*
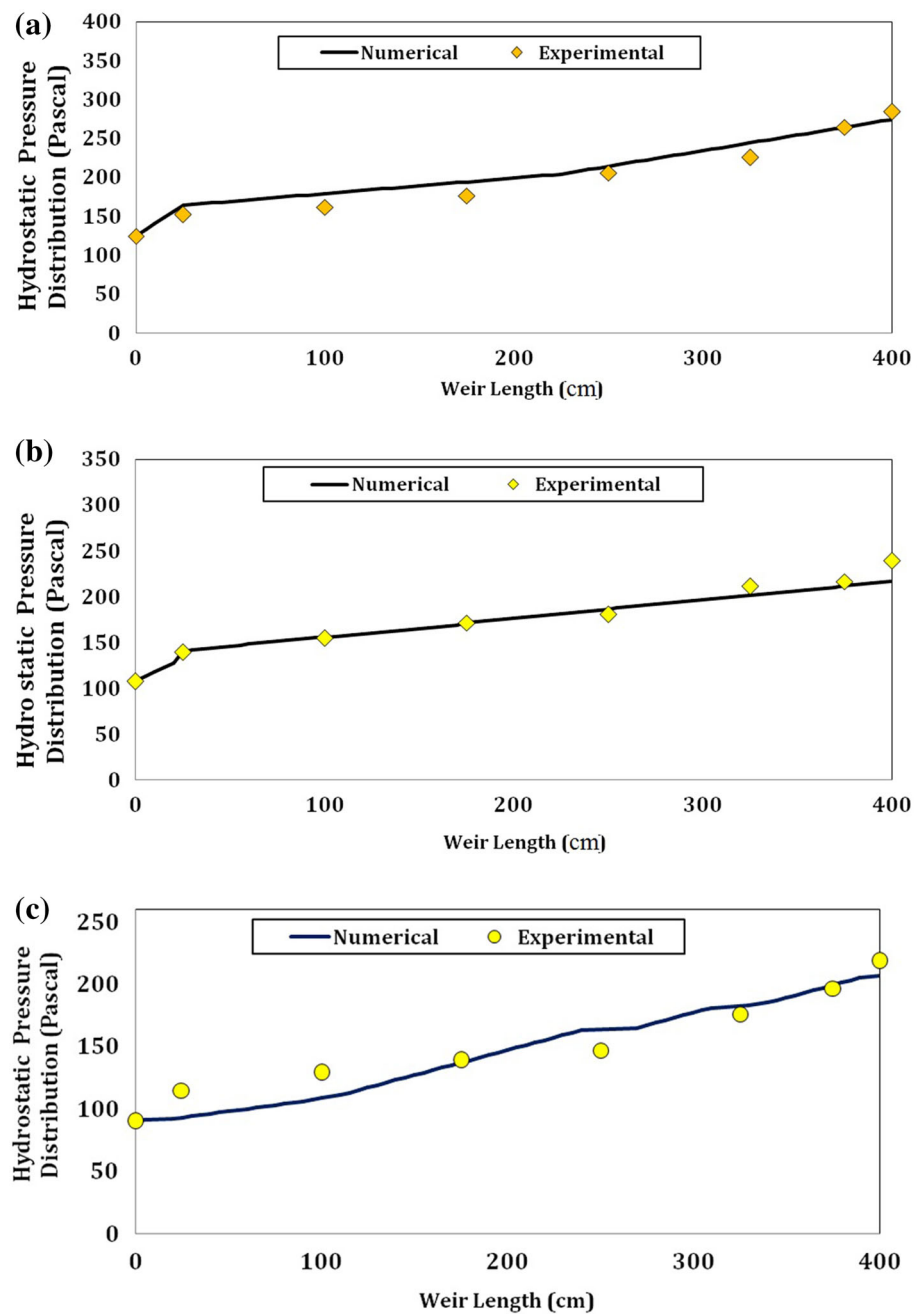

(a)

(b)

(c)

Table 1 Measured and predicted flow parameters

	Description	Units	Simulation results	Experimental results
1	Inlet discharge (Q_1)	L/s	110	110
2	Downstream discharge (Q_2)	L/s	71.42	69.13
3	Total weir outflow discharge (Q_3)	L/s	38.58	40.87
4	Discharge ratio (Q_3/Q_1)	–	0.350	0.371
5	Upstream Froude number (Fr$_1$)	–	0.53	0.49
6	Upstream water depth (y_1)	cm	12.21	12.32

The standard k-ε The standard *k-ε* model has been the most widely used two-equation model since it was introduced by Launder and Spalding [31]. The standard *k-ε* model is a semi-empirical model based on model transport equations

Table 2 Grid information and downstream discharge computed from the solutions

Grid	Normalized grid spacing (r)	p	Downstream discharge (L/s)
1	1	1.53 > 2	71.73
2	2		71.65
3	4		71.42

for the turbulence kinetic energy (k) and its dissipation rate (ε) [32].

3.2 Free Surface Tracking (Volume of Fluid Method)

Several methods have been used to approximate free surface. A simple, but powerful method is volume of fluid (VOF) [33]. This method is shown to be more flexible and efficient than other methods for treating complicated free surface. VOF model is designed for two or more immiscible fluids, where the position of the interface between the fluids is of interest. In each cell of a mesh, it is usual to use only one value for each dependent variable, defining the fluid state. If a function named F is assumed, the average value of F in a cell would then represent the fractional volume of the cell occupied by a certain fluid. In particular, a unit value of F would correspond with a cell full of a certain fluid, while a zero value would indicate that the cell contained no fluid. Cells with F values between zero and one must then contain a free surface. For air–water flow field, a single set of momentum equation is shared by air and water and the volume fraction of each fluid in each computational cell is tracked throughout the domain. In each cell, the sum of the volume fractions of air and water is unity. So an additional variable, the volume fraction of air or water is introduced. If F_w denotes the volume fraction of water, then the volume fraction of air F_a can be expressed as

$$F_a = 1 - F_w \qquad (2)$$

The value of F_a in a cell represents the fractional volume of the cell occupied by air. In particular, $F_a = 1$ will correspond to a cell full of air, while $F_a = 0$ will indicate that the cell is full of water. Therefore, the interface information can be known according to the value of F_a. In summary, the volume of fluid (VOF) technique can locate free surface as well as a distribution of air concentration because it follows regions rather than surfaces [34].

3.3 Boundary Conditions and Mesh Geometry

The mesh consists of 121,195 cells, 330,669 faces and 111,765 nodes. The upstream boundary condition in y direction was defined as "Pressured-inlet." In order to use

pressured-inlet as the upstream boundary condition, the open channel term is activated. By activation of this module, pressure inlet boundaries require the velocity magnitude to calculate the dynamic pressure at the boundary and also free surface level (fluid depth). These values were imported from the mean flow velocity as well as mean fluid depth of flow at the upstream of the side weir in the experiment. The total height will be calculated as:

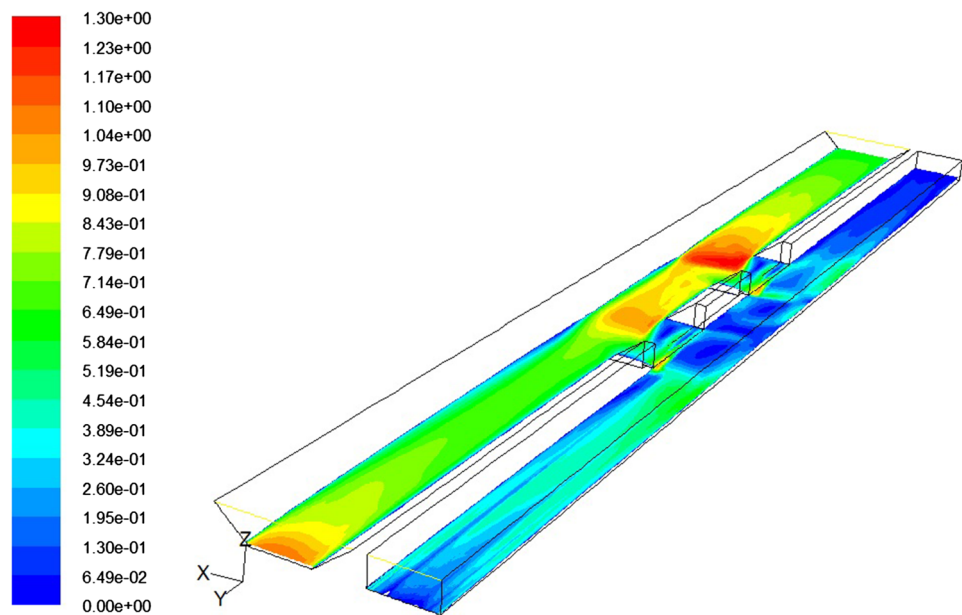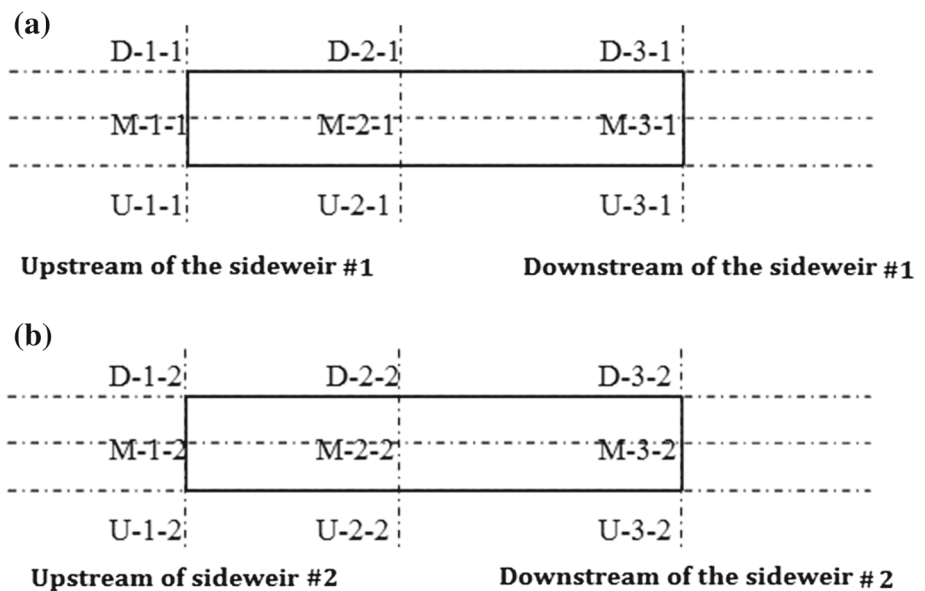$$Y_{\text{total}} = y + (V^2/2g) \qquad (3)$$

where V is the velocity magnitude, y is the upstream fluid depth and g is the gravity magnitude.

"Pressured-outlet" boundary was set at the downstream of y direction. Boundary condition for the z direction was labeled as "symmetry," which implies that identical flows occur on the other side of the boundary, and hence, there is no drag. The "wall function" was applied in other parts of the model. The wall roughness was set using the roughness height computed from Manning's formula. The acceleration of gravity was applied in the negative z-direction. The evolution in time was used as a relaxation to the final steady state. The steady state was checked through monitoring the flow kinetic energy. Physical model configurations were simulated during 48 s. It should be mentioned that the simulation was done for the inlet discharge of 110 L/s. Figure 7 shows a view of the simulated side weirs. In this numerical solution, the flow equations are discretized with the nonlinear third-order quadratic upwind interpolation of convective kinematics (QUICK) scheme of Leonard [35]. The discrete equations are solved in an iterative manner to steady state using the semi-implicit method for pressure-linked equations (SIMPLE) algorithm of Patankar and Spalding [36]. The 3D free water surface model adopted the standard k-ε turbulence model and the volume of fluid (VOF) to represent the sharp interface between the air and water.

4 Model Validation

In order to verify the results of the numerical modeling, they are compared with the results of the experimental model under the same conditions [23]. The result of the comparison between the simulated longitudinal pressure distributions over the side weir with the experimental data, at axis a–a, b–b and c–c, is shown in Fig. 8a–c, respectively. These results show that the predictions of the present numerical simulation compare well with the present experimental results. These data are in very good agreement with the numerical model predictions marked by the solid lines.

Table 1 clearly demonstrates the comparison between the predicted and measured flow rates for the single-weir case in order to demonstrate the validity of the model in estimating

Fig. 9 Variation of the velocity magnitude in the main channel

Fig. 10 locations of sections over the **a** first and **b** second side weir

(a)

Upstream of the sideweir #1   Downstream of the sideweir #1

(b)

Upstream of sideweir #2   Downstream of the sideweir # 2

flow rates. The discharge coefficients used in the estimation of discharge rates are also mentioned in the table.

4.1 Numerical Uncertainty

Numerical uncertainty is defined as the estimated amount or percentage by which an observed or calculated value may differ from the true value. There are three reasons for numerical uncertainty: (1) input uncertainty, (2) model uncertainty and (3) numerical uncertainty. Input uncertainty emerges from inaccurate definition of input parameters. So, this uncertainty is not related to the model at all. Model uncertainty is the outcome of different model formulations. Numerical uncertainty results from the influence of discretization and iterative con-

vergence errors. This is the only uncertainty that cannot be eliminated, but minimized or restricted in a simulation. For instance, input uncertainty has the potential to be eliminated or made a second-order effect through improved definition of the input parameter (i.e., a better-measured value) or model uncertainty can be minimized or potentially be eliminated by the use of an enhanced models. However, numerical uncertainty is a first-order effect that has no chance to be utterly eliminated. The only approach is to develop helpful error predictors which are able to calculate this numerical uncertainty. Systematic grid refinement studies are the most common approaches used in assessing numerical accuracy of a simulation. One of the most well-known approaches for grid refinement is Roache's grid convergence index (GCI). The

Fig. 11 Water surface profile over the side weirs at sections **a** U.1.2–U.3.2 and U.1.1–U.3.1, **b** M.1.2–M.3.2 and M.1.1–M.3.1, and **c** D.1.2–D.3.2 and D.1.1–D.3.1
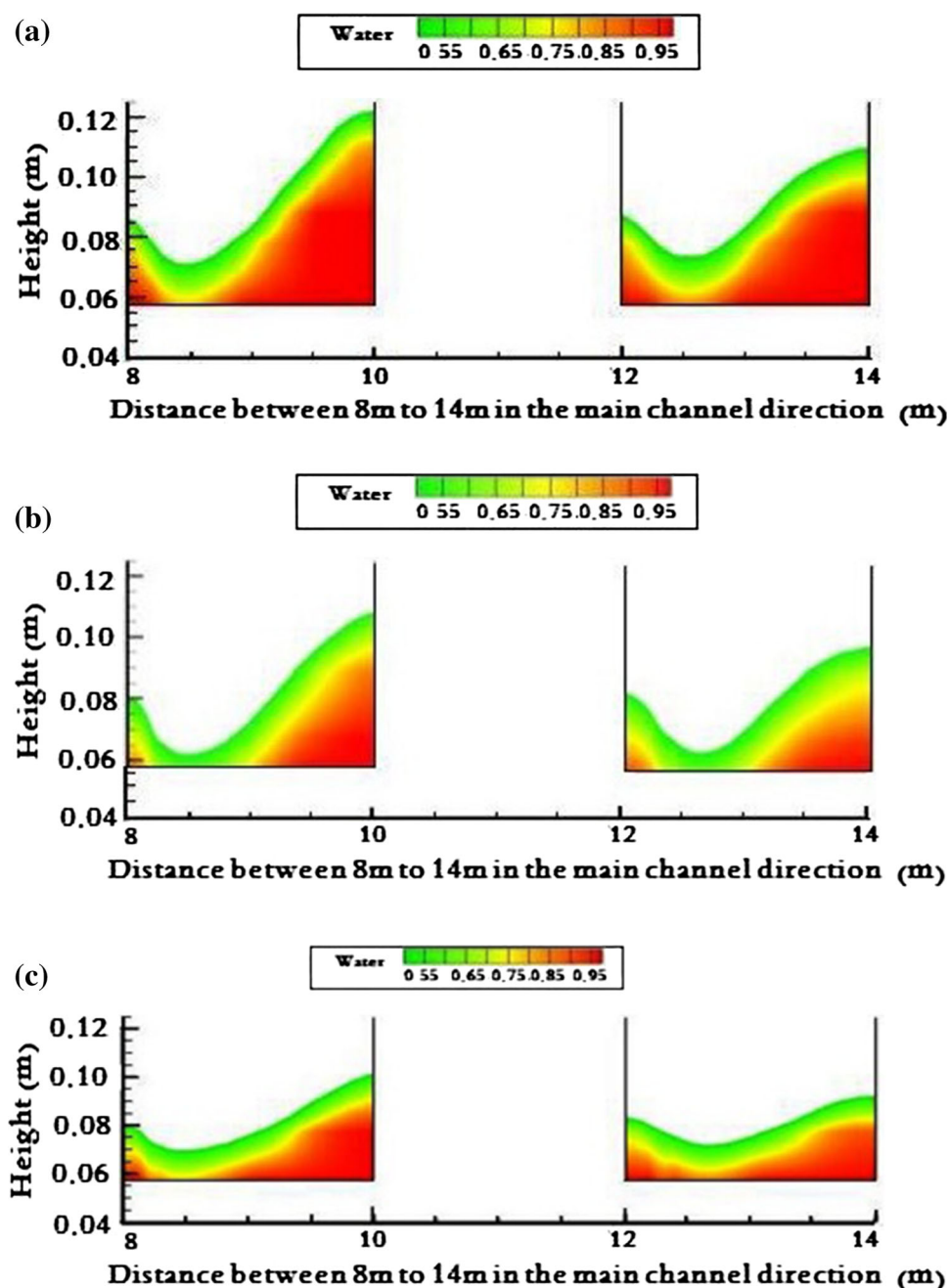
GCI value represents the resolution level and how much the solution approaches the asymptotic value. If the formal order of accuracy is not known, then three different (twice halved or doubled) grids and solutions are required to determine the order of the method and the error [37]. GCI for two different girds is defined as:

$$\mathrm{GCI}_{i+1,i} = \frac{F_s}{r^P - 1} \left| \varepsilon_{i+1,i} \right| \tag{4}$$

where F_s is a safety factor. Following Wilcox [38], the safety factor (F_s) selected for this study is 1.25, r is the ratio of grid

spacing on the two grids. From the above equation, P and ε are defined as:

$$p = \frac{\ln\left(\frac{f_3 - f_2}{f_2 - f_1}\right)}{\ln(r)} \tag{5}$$

where f_1, f_2 and f_3 are the outcome of simulation results from three different grids. It should be mentioned that the theoretical order of convergence is $p = 2.0$. The difference is most likely due to grid stretching, grid quality, nonlinearities

Fig. 12 Water surface profile over the side weirs
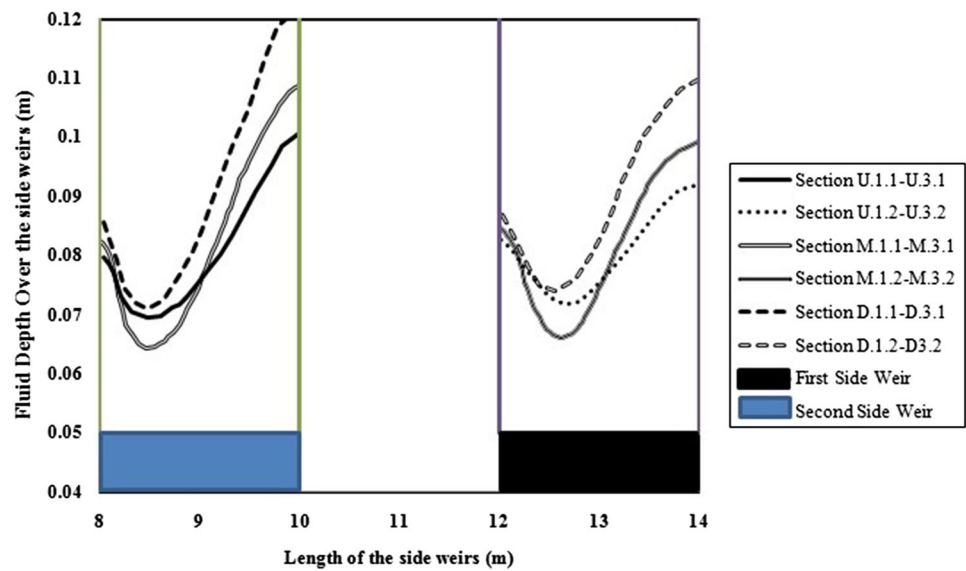
in the solution, presence of shocks, turbulence modeling and perhaps other factors.

$$\varepsilon_{i+1,i} = \frac{f_{i+1} - f_i}{f_i} \tag{6}$$

Richardson extrapolation gives the exact solution as:

$$f_{h=0} \cong f_1 + \frac{f_1 - f_2}{r^{p-1}} \tag{7}$$

where h is grid spacing. In order to ascertain the numerical accuracy of the simulation, this parameter should be close to one for two successive grids:

$$\frac{\text{GCI}_{i+1,i+2}}{r^p \text{GCI}_{i,i+1}} \cong 1 \tag{8}$$

In this paper, the flow field is computed on three grids, each with twice the number of grid points in the x and y coordinate directions as the previous grid. The number of grid points in the z direction remains the same. Since the flow is axisymmetric in the z direction, it was considered that the finer grid to be double the next coarser grid. In this paper, the outflow discharge from the main channel (71.42 L/s) is set as the target function.

Table 2 indicates the grid information and downstream discharge computed from the solutions. Each solution was properly converged with respect to iterations. The column indicated by "normalized grid spacing" is the spacing normalized by the spacing of the finest grid.

$$p = \frac{\ln\left(\frac{f_3 - f_2}{f_2 - f_1}\right)}{\ln(r)} = \frac{\ln\left(\frac{71.42 - 71.65}{71.65 - 71.73}\right)}{\ln(2)} = 1.53 < 2 \tag{9}$$

$$\text{GCI}_{12} = \frac{1.25}{2^{1.53} - 1} \left(\frac{71.73 - 71.65}{71.73}\right) \times 100 = 0.073\% \tag{10}$$

$$\text{GCI}_{23} = \frac{1.25}{2^{1.53} - 1} \left(\frac{71.65 - 71.42}{71.42}\right) \times 100 = 0.21\% \tag{11}$$

$$\frac{\text{GCI}_{23}}{r^p \text{GCI}_{12}} = \frac{0.21}{2^{1.53} \times 0.073} = 0.996 \approx 1 \tag{12}$$

which is approximately one and indicates that the solutions are well within the asymptotic range of convergence

4.2 Simulation Convergence

There are several ways to check whether the simulation is converged or not. The most general is to check the residuals for each variable being solved. Only upon looking at the drop in residuals can we get an indication of the overall level of convergence. The rule is to look at the first residual or the maximum residual calculated and then look for 3–5 orders of magnitude drop from there. In this simulation, the maximum residual calculated was 1 at the beginning. However, after approximately 3900 iterations, it leads to 0.0001 which shows that the solution will converge. In other words, the solution does not change anymore after approximately 3900 iterations.

5 Results and Discussion

To explain different stages of simulation, it should be stated that firstly, higher discharged flow diverts into the lateral channel through the first side weir, and then, flow with lower discharge passes through the second side weir. The

Fig. 13 Water surface profile over the **a** first and **b** second side weir
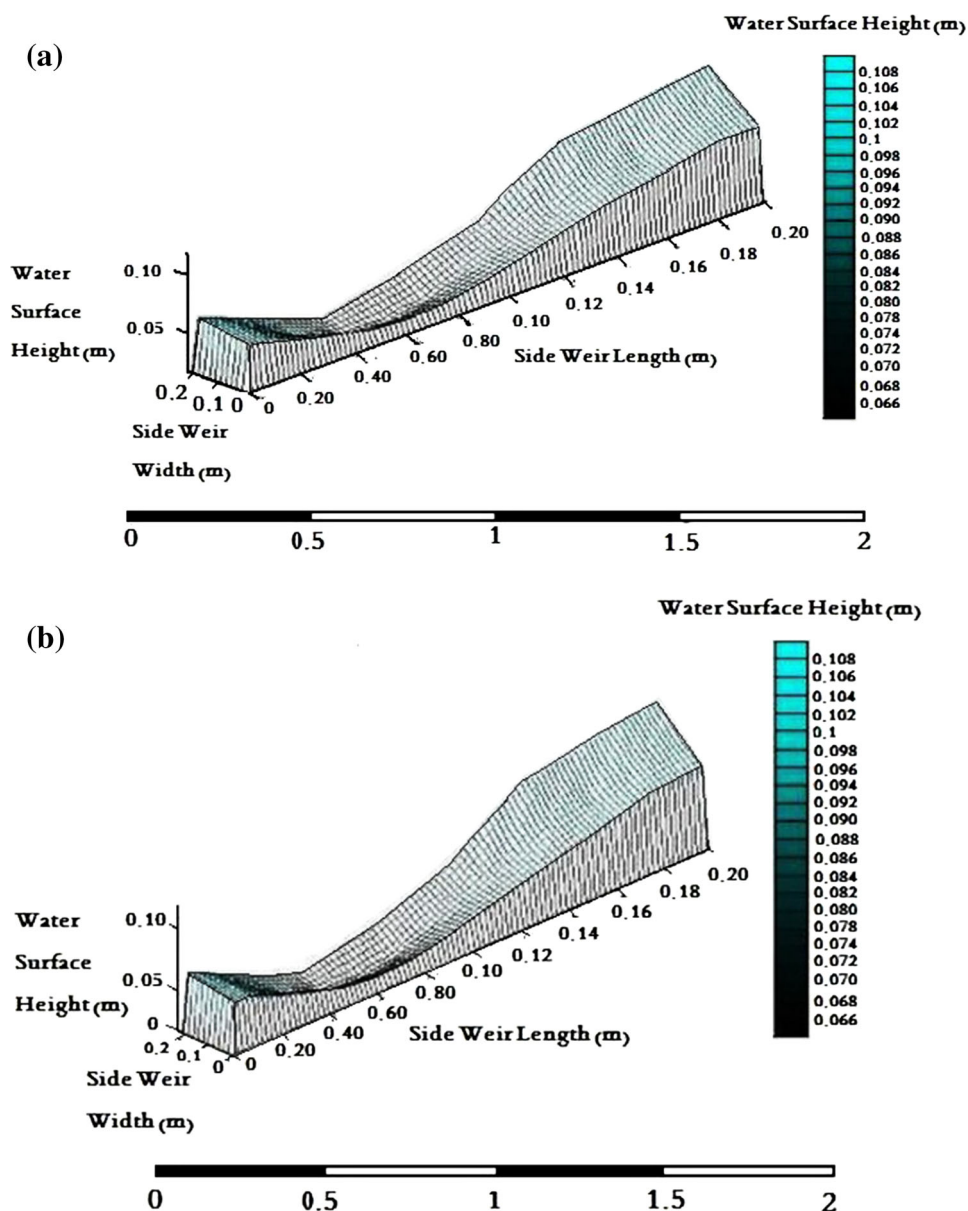
amount of flow diverted into the lateral channel from both side weirs joins together and moves toward the downstream and upstream of the lateral channel (because of longitudinal slope). Since the upstream boundary is defined as wall, flow would gather at the upstream of the lateral channel and moves downward gradually until it is passed through the downstream boundary. Figure 9 shows variation of the velocity magnitude in the main channel. As it is clear, the flow at the upstream and the downstream of the side weir is subcritical except in the main channel across the first side weir showing velocity values over 1 m/s. So, the water surface profiles over the side weirs are similar to Fig. 3a.

In order to analyze flow pattern over the side weirs more specifically, 9 points are signified over each side weir, dividing the side weirs into three transverse and longitudinal

sections (Fig. 10a, b). The letters U, M and D stand for the upstream, middle and downstream of the side weir, respectively. The first number after the letters represents the number of section and the second one represents the number of the side weir.

Figure 11a–c shows the longitudinal water surface profile over the side weirs. It is clear that the flow pattern increases through the downstream of both of the side weirs exactly like the experiments representative of subcritical flow in the main channel, as mentioned above. It also shows that the intensity of water surface profile decreases from U.1.i–U.3.j section to D.1.i–D.3.j section ($i, j = 1, 2$) for each side weir. It is also clear that water surface profile over the first side weir is higher than the second side weirs. In order to better clarify

Fig. 14 Longitudinal water surface profile along the main channel in two side weir simulations
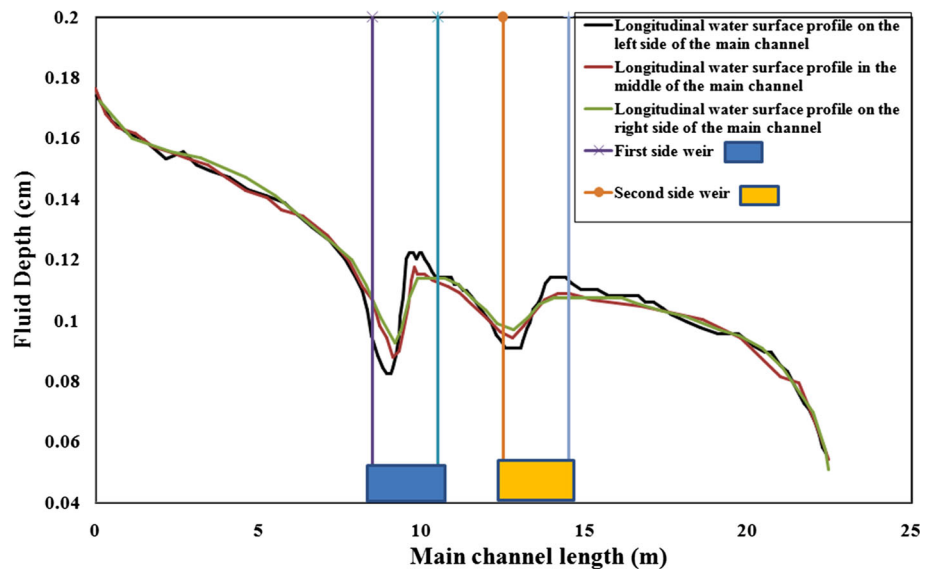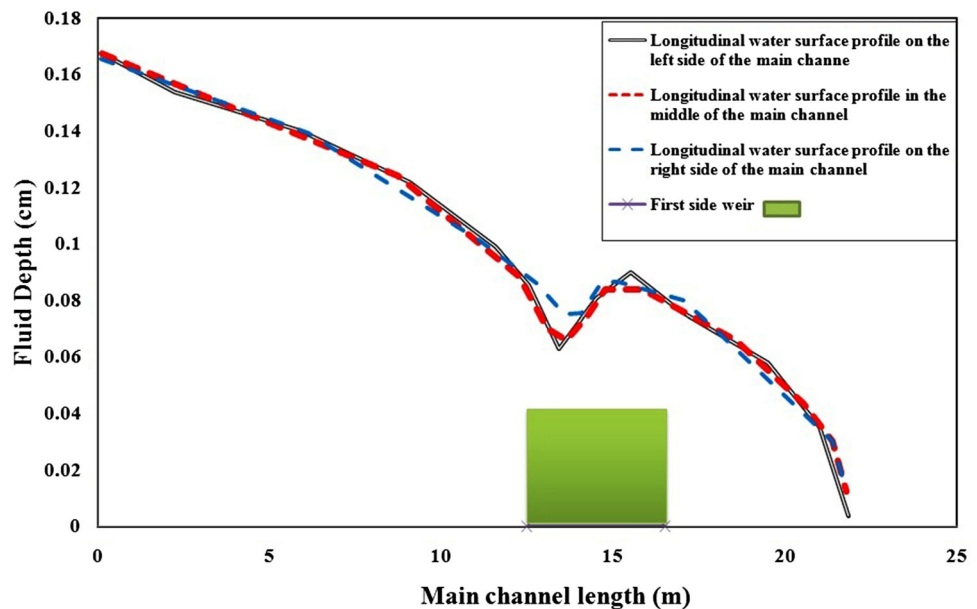

Fig. 15 Longitudinal water surface profile along the main channel in single side weir simulation

the water surface profiles, all of the longitudinal profile of the side weirs are gathered in Fig. 12.

Figure 13a, b also shows the water surface profile over the crest of side weirs. As it is clear in figures, the amount of discharge over the first side weir is significantly greater than the one over the second one.

Figures 14 and 15 show longitudinal water surface profile along the main channel in the left side of main channel (near the side weirs), in the middle of the main channel and in the right side of the main channel for both single and two side weir simulations. As it can be seen, the flow near the side weirs has become more instable and more turbulence. However, flow is nearly stable before and after and in the middle of the side weirs. The reason that the water surface

in the main channel deceases and then increases is due to the existence of side weir. Since the flow before and after the side weirs is subcritical, the flow pattern over the side weirs follows type I condition which was explained before. The flow type over the side weirs affects the flow in the main channel and makes it change similar to flow over the side weirs. However, the intensity of changes increases by getting closer to the side weir. As Figs. 14 and 15 show, the profiles which are related to the left side of the main channels are subjected to higher fluctuation. In other words, the range of changes decreases from the left side of main channel to the right side of the main channel

The transverse water surface profile over the side weirs at the mentioned sections is compared with the experimental

Fig. 16 Transverse water surface profile over the side weirs at sections U.1.1–D.1.1 & U.1.2–D.1.2 and section O–P in the experiments
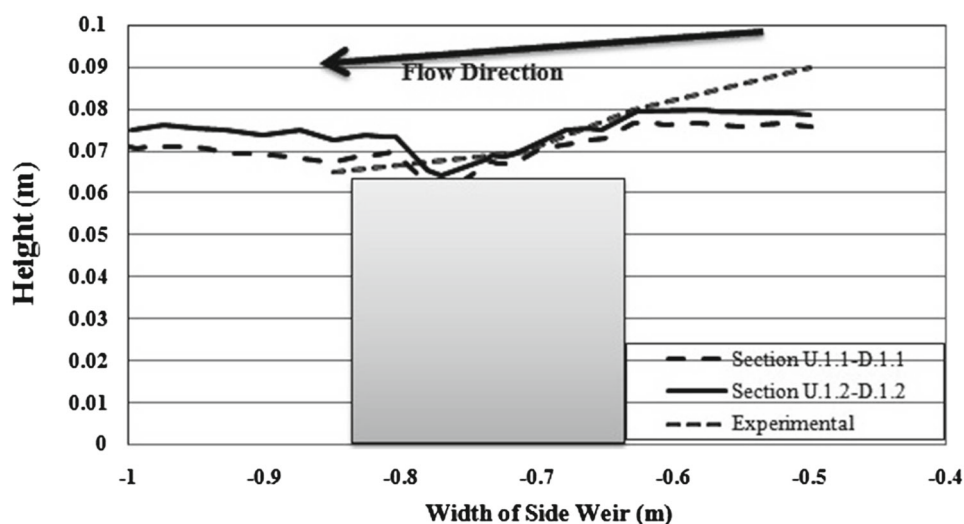

Fig. 17 Transverse water surface profile over the side weirs at sections U.2.1–D.2.1 & U.2.2–D.2.2 and section G–H in the experiments
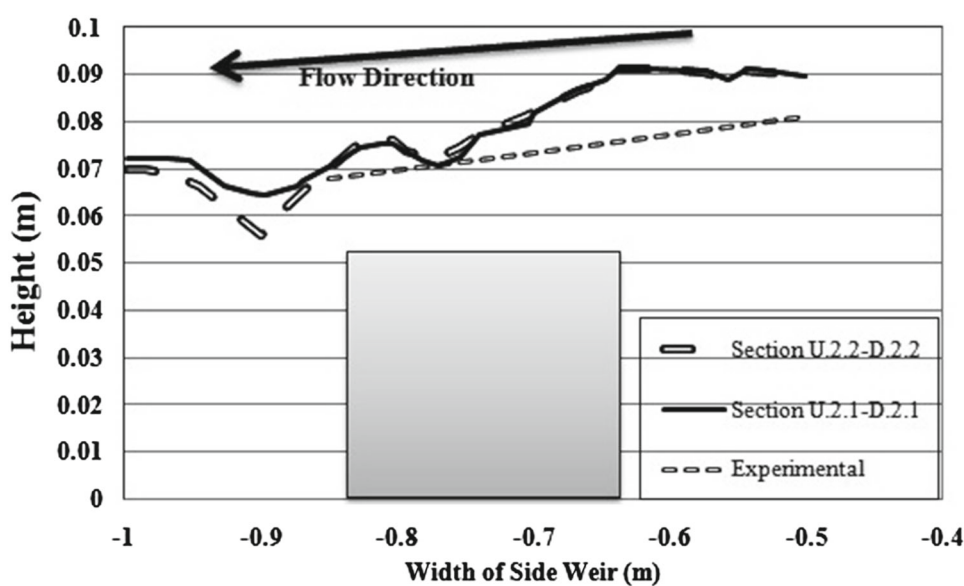

Fig. 18 Transverse water surface profile over the side weirs at sections U.3.1–D.3.1 & U.3.2–D.3.2 and section A–B in the experiments
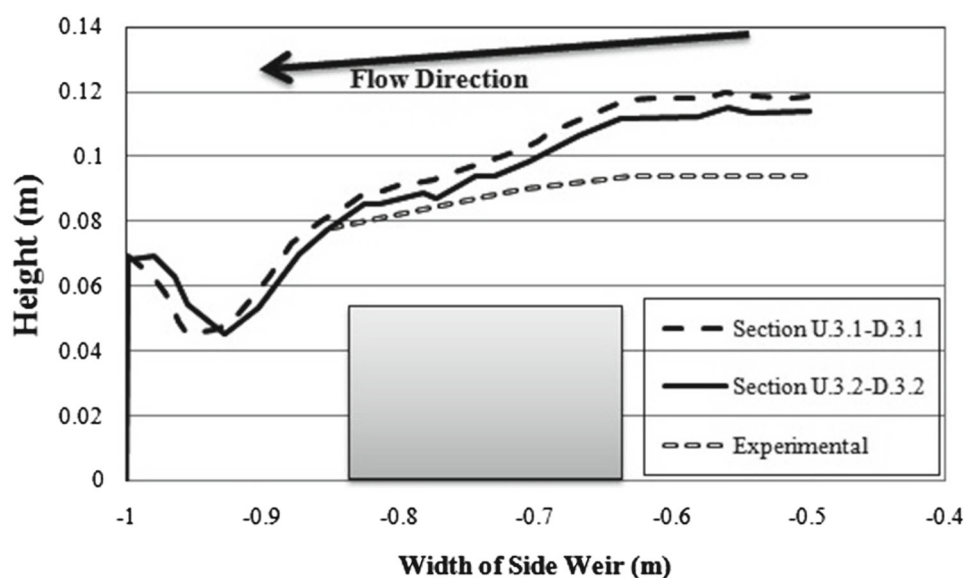
Table 3 Comparison between the results of single and two side weir simulations with experimental results

Description	Units	Single side weir simulation results	4 m weir	Two side weir simulations results
Inlet discharge (Q_1)	L/s	110	110	110
Downstream discharge (Q_2)	L/s	71.42	69.13	50.57
First weir outflow discharge (Q_{31})	L/s	38.58	40.87	32.67
Second weir outflow discharge (Q_{32})	L/s	–	–	26.76
Total weir outflow discharge (Q_3)	L/s	38.58	40.87	59.43
Upstream Froude number (Fr_1)	–	0.53	0.49	0.46
Upstream water depth (y_1)	cm	12.21	12.32	12.78

one. As it is clearly shown in Fig. 16, 17 and 18, transverse water surface profiles of the simulated side weirs with shorter lengths are higher than the water surface profile of the side weir in the experiments with the length of 4 m. Table 3 shows a comparison between the results of single and two side weir simulations with experimental results. As Table 3 shows, the first weir of the double weir simulation gives lower amount of flow rate compared to the single side weir and the 4 m weir. This is completely rational since it has smaller size. However, the second side weir also passes 26.76 L/s. By adding the amount of outflow discharge from the first and second side weirs, a higher amount of outflow discharge is reached (59.43 L/s) compared to the single side weir simulation and the 4 m weir. Therefore, this important result shows that by using two side weirs instead of a single side weir, it is highly possible to get higher outflow discharge.

6 Conclusions

As the experimental data for the case in which there was a side weir with the length of 4 m existed, the flow over two side weirs with shorter lengths was numerically investigated. The main objective of this paper was to reveal that to what extent a numerical model can be useful, practically, to investigate the different hydraulic phenomenon from different aspects without having necessity for extra experiments. This investigation shows that installation of two shorter side weirs instead of one long side weir will increase the amount of lateral outflow. According to the obtained results, the amount of discharge entering the first side weir is higher than the second one, and if there had been more side weirs, the rate of flow would have expectedly decreased toward the downstream of the main channel. It was seen that in the two side weir simulations, outflow discharge amounts of 32.67 and 26.76 L/s were passed from the first and second side weir, respectfully. Therefore,

higher amount of total outflow discharge was obtained compared to the experimental one. Moreover, water surface over the first simulated side weir was higher than the values of the second side weir. Water surface profiles on the left, right and the middle of the side weir were also investigated. It was seen that these profiles undergo some fluctuation along the main channel which are related to the water surface profile over the side weir.

7 Suggestion

It is not distinctive that to what extend the outflow discharge would change by increasing or decreasing the space between 2 m weirs; therefore, it is suggested to increase or decrease this space and compare it with the current results.

References

1. De Martonne, E.: Aréisme et indice artidite. Comptes Rendus de L'Acad Sci. Paris **182**, 1395–1398 (1926)
2. De Marchi, G.: Saggio di teoria de funzionamente degli stramazzi letarali. L'Energia Elettr. **11**(11), 849–860 (1934)
3. Ackers, P.: A theoretical consideration of side weirs as storm water overflows. In: Proceedings of the ICE, vol. 6, pp. 250–269. London (1957)
4. Collings, V.K.: Discharge capacity of side weir. In: Proceedings of the ICE—Civil Engineering, vol. 6, pp. 288–304. London, England (1957)
5. Frazer, W.: The behavior of side weirs in prismatic rectangular channel. In: Proceedings of the ICE—Civil Engineering, vol. 6, pp. 305–327, London, England (1957)
6. Subramanya, K.; Awasthy, S.C.: Spatially varied flow over side weirs. J. Hydraul. Div. **98**(1), 1–10 (1972)
7. Nandesamoorthy, T.; Thomson, A.: Discussion of spatially varied flow over side weir. J. Hydraul. Eng. ASCE **98**(12), 2234–2235 (1972)
8. Singh, R.; Manivannan, D.; Satyanarayana, T.: Discharge coefficient of rectangular sides. J. Irrig. Drain. Eng. ASCE **120**(4), 814–819 (1994)

9. Yu-Tech, L.: Discussion of spatially varied flow over side weir. J. Hydraul. Eng. ASCE **98**(11), 2046–2048 (1972)

10. Cheong, H.: Discharge coefficient of lateral diversion from trapezoidal channel. J. Irrig. Drain. Eng. **117**(4), 461–475 (1991)

11. El-Khashab, A.; Smith, K.V.H.: Experimental investigation of flow over side weirs. J. Hydraul. Eng. ASCE **102**(9), 1255–1268 (1976)

12. Uyumaz, A.; Muslu, Y.: Flow over side weir in circular channels. J. Hydraul. Eng. ASCE **111**(1), 144–160 (1985)

13. Hager, W.H.: Lateral outflow over side weirs. J. Hydraul. Eng. ASCE **113**(4), 491–504 (1987)

14. Hager, W.H.: Supercritical flow in circular-shaped side weirs. J. Irrig. Drain. Eng. ASCE **120**(1), 1–17 (1994)

15. Helweg, O.J.: Microcomputer Applications in Water Resources. Prentice Hall PTR, Upper Saddle River, NJ (1990)

16. Agaccioglu, H.; Yüksel, Y.: Side weir flow in curved channels. J. Irrig. Drain. Eng. ASCE **124**(3), 163–175 (1998)

17. Venutelli, M.: Method of solution of non-uniform flow with the presence of rectangular side weir. J. Irrig. Drain. Eng. ASCE **134**(6), 840–846 (2008)

18. Durga Rao, K.H.V.; Pillai, C.R.S.: Study of flow over side weirs under supercritical conditions. Water Resour. Manag. **22**(1), 131–143 (2008)

19. Ranga Raju, K.G.; Prasard, B.; Gupta, S.K.: Side weir in rectangular channel. J. Hydraul. Div. ASCE **105**(5), 547–554 (1979)

20. Kumar, C.P.; Pathak, S.K.: Triangular side weirs. J. Irrig. Drain. Eng. ASCE **113**(1), 98–105 (1987)

21. Borghei, M.; Jalili, M.R.; Ghodsian, M.: Discharge coefficient for sharp crested side weir in subcritical flow. J. Hydraul. Eng. ASCE **125**(10), 1051–1056 (1999)

22. Kaya, N.; Emiroglu, M.; Agaccioglu, H.: Discharge coefficient of a semi-elliptical side weir in subcritical flow. Flow Meas. Instrum. **22**, 25–32 (2011)

23. Namaee, M.R.; Jalaledini, M.S.; Habibi, M.; Yazdi, S.R.S.; Ghafouri Azar, M.: Discharge coefficient of a broad crested side weir in an earthen channel. Water Sci. Technol. Water Supply **13**(1), 166–177 (2013)

24. Isel, S.; Dufresne, M.; Fischer, M.; Vazquez, J.: Assessment of the overflow discharge in complex CSO chambers with water level measurements—on-site validation of a CFD-based methodology. Flow Meas. Instrum. **35**, 39–43 (2014)

25. Chen, Z.; Han, S.; Zhou, F.Y.; Wang, K.: A CFD modeling approach for municipal sewer system design optimization to minimize emissions into receiving water body. Water Resour. Manag. **27**(7), 2053–2069 (2013)

26. Isel, S.; Dufresne, M.; Bardiaux, J.B.; Fischer, M.; Vazquez, J.: Computational fluid dynamics based assessment of discharge-water depth relationships for combined sewer overflows. Urban Water J. **11**(8), 631–640 (2014)

27. Lipeme Kouyi, G.L.; Vazquez, J.; Gallin, Y.; Rollet, D.; Sadowski, A.G.: Use of 3D modelling and several ultrasound sensors to assess overflow rate. Water Sci. Technol. **51**(2), 187–294 (2005)

28. Namaee, M.R.; Rostami, M.; Jalalediny, M.S.; Habibi, M.: A 3-dimensional simulation of flow over a broad crested side weir. In: Advances in Hydro Informatics, pp. 511–523. Springer (2014)

29. Namaee, M.R.: A numerical investigation of flow over a side weir based on the experimental data. Aust. J. Water Resour. **18**(2), 1–10 (2015)

30. May, R.W.P.; Bromwich, B.C.; Gasowski, Y.; Rickard, C.E.: Hydraulic Design of Side Weirs. Thomas Telford Publishing, London (2003)

31. Launder, B.E.; Spalding, D.B.: The numerical computation of turbulent flows. Comput. Methods Appl. Mech. Eng. **3**(2), 269–289 (1974)

32. Launder, B.E.; Spalding, D.B.: Lectures in Mathematical Models of Turbulence. Academic Press, London (1972)

33. Hirt, C.W.; Nicholas, B.D.: Volume of fluid (VOF) method for the dynamics of free boundaries. J. Comput. Phys. **39**(1), 201–225 (1981)

34. Dong, Z.Y.; Lee, J.H.W.: Numerical simulation of skimming flow over mild stepped channel. J. Hydrodyn. Ser. B **18**(3), 367–371 (2006)

35. Leonard, B.P.: A stable and accurate convective modeling procedure based on quadratic up-stream interpolation. Comput. Methods Appl. Mech. Eng. **19**, 59–98 (1979)

36. Patankar, S.V.; Spalding, D.B.: A calculation procedure for heat, mass and momentum transfer in three-dimensional parabolic flows. Int. J. Heat Mass Transf. **15**(10), 1787–1806 (1972)

37. Freitas, C.J.: The issue of numerical uncertainty. Appl. Math. Model. **26**, 237–248 (2002)

38. Wilcox, D.C.: Turbulence Modeling for CFD, 3rd edn. DCW Industries, Inc., La Canada, CA (2006)